Aldol condensation of citral with acetone on MgO and alkali-promoted MgO catalysts

V.K. Díez, C.R. Apesteguía, J.I. Di Cosimo *

Catalysis Science and Engineering Research Group (GICIC), Instituto de Investigaciones en Catálisis y Petroquímica-INCAPE-(UNL-CONICET), Santiago del Estero 2654, (3000) Santa Fe, Argentina

Abstract

The liquid-phase synthesis of pseudoionones (PSs) by cross-aldol condensation of citral with acetone was studied on alkali-promoted MgO catalysts. Alkaline metals (A), including Li, Na, K, and Cs, were added to a high-surface area MgO in A/Mg molar ratios of up to 0.01. Promoters of greater ionic radius than Li blocked the catalyst pores of MgO, causing a decrease in both surface area and catalyst activity. In contrast, the addition of Li enhanced the PS yield of parent MgO. This beneficial effect of Li was further investigated by preparing, characterizing, and testing several Li/MgO catalysts with different Li loadings. The results were interpreted in terms of the structural, textural, and basic properties of the resulting oxides. Li loadings of up to 0.5 wt% increased the total base site density of parent MgO mainly by increasing the density of very active strong base sites (low coordination oxygen anions), and thereby promoted the PS formation rate. Increasing the Li concentration further caused particle agglomeration and formation of unreactive carbonates that block the active sites. The citral/acetone aldol condensation mechanism on Li–MgO catalysts was also investigated, and a Langmuir–Hinshelwood–Hougen–Watson kinetic expression was developed to account for the initial PS formation rate and to interpret experimental data. It was found that the rate-determining step is the abstraction of the α-proton from the acetone molecule that occurs on strong Brönsted base sites. A PS yield of 93% was obtained at 353 K with a catalyst/citral weight ratio of 0.2 for the 0.5 wt% Li/MgO catalyst at the end of the 6-h catalytic run.
© 2006 Elsevier Inc. All rights reserved.

Keywords: Pseudoionone synthesis; Citral; Aldol condensation; MgO; Alkaline metals; Base catalysis; Acetone

1. Introduction

Citral (3,7-dimethyl-2,6-octadien-1-al) is a widely used key building block in fine chemicals, particularly in the production of vitamins A and E, as well as carotenoids and an extended range of aroma chemicals [1]. The worldwide demand for citral has increased significantly in recent years due to increasing needs for high-quality products in animal nutrition, food production, and innovative cosmetics. Consequently, fine chemistry companies have invested in citral and its derivatives to expand the production scale and meet market demand. For example, in 2004 BASF inaugurated, at its Ludwigshafen, Germany site, a world-scale plant with an annual capacity of 40,000 metric tons, replacing an existing 10,000 metric tons/year capacity plant. This new citral production plant uses a more ecologically and economically favorable process that starts with cheaply available isobutene and formaldehyde [2].

Among citral-derived compounds, pseudoionones (PSs) are valuable acyclic precursors for the synthesis of α- and β-ionones, which are extensively used in pharmaceuticals and fragrances. The β-ionone isomer is the preferred reactant for different synthesis processes leading to vitamin A, whereas α-ionone is in high demand in the fragrance industry because of its sweet floral scent, reminiscent of violets [3].

Currently, PSs are commercially produced via the aldol condensation of citral with acetone in a liquid-phase process involving the use of diluted bases, such as NaOH, Ba(OH)$_2$, and LiOH. This process entails concerns related to high toxicity, corrosion, and disposal of spent base materials [4,5]. The consecutive cyclization of PSs to yield α- and β-ionones is
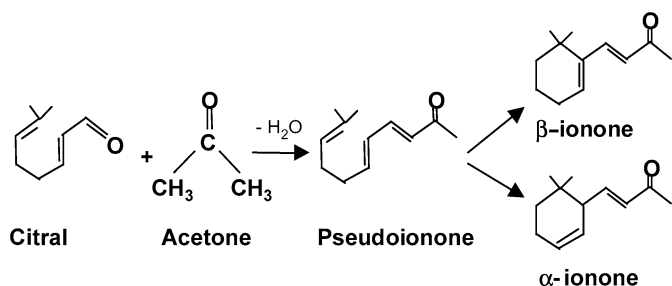
Scheme 1. Reaction sequence for pseudoionone and ionone synthesis.

catalyzed by strong liquid acids [1]. The two-step process for ionone synthesis is depicted in Scheme 1.

Increasing research work has recently been performed to find suitable and recyclable solid catalysts for efficiently promoting the liquid-phase aldol condensation of citral with acetone, with the aim of developing an environmentally benign process for producing PSs. Climent et al. [6] reported that this reaction is poorly catalyzed using acid zeolites or bifunctional acid-base aluminophosphates (ALPO). In contrast, using solid bases, such as MgO and Mg–Al mixed oxides, may selectively produce PSs [6,7]. Others [8–10] have noted that Mg–Al anionic clays of hydrotalcite structure with Mg/Al = 2–3 (molar ratio) also preferentially form PSs, although the catalyst activity and selectivity are greatly affected by both the synthesis procedure and the activation steps. In particular, Climent et al. [9] reported high PS yields on anionic clays prepared under non-conventional microwave irradiation or sonication methods and subsequent careful rehydration with decarbonated water. Recently, Abelló et al. [10] and Jablonski et al. [11] reported a positive promoting effect of alkaline metals on Mg–Al hydrotalcites and MgO, respectively, for PS synthesis.

These previous works showed that anionic clays and single or mixed oxides with basic properties are potential solid catalysts for aldol condensation of citral with acetone. However, efforts devoted to elucidate the exact requirements of the base site that promotes this reaction in terms of density and strength, and the role played by the chemical nature and concentration of the accompanying Lewis acid site (the metal cation) in the generation of the base sites as well as in the surface coordination of both reactants, are still needed.

In this work, we study the citral/acetone reaction on alkali-doped MgO catalysts prepared by conventional impregnation method. We focus in particular on Li-promoted MgO, taking into account that we have previously observed that Li-containing MgO is highly active for acetone condensation reactions in the gas phase [12]. We carry out a systematic study of the effect of Li concentration on the structural, textural, and basic properties of the resulting Li-doped MgO catalysts using various experimental techniques. We also correlate those properties with the catalytic performance for citral/acetone aldol condensation and postulate a reaction mechanism for this process. Our goals are to identify the active site operating under our experimental conditions and to provide an interpretation for the effect of Li in selectively promoting PS formation.

2. Experimental

2.1. Catalyst synthesis

Magnesium oxide was prepared by hydration with distilled water of low-surface area commercial MgO (Carlo Erba, 99%, 0.2% Na, 27 m^2/g). Then, the resulting $Mg(OH)_2$ was decomposed and stabilized at 773 K in a N_2 flow for 18 h to obtain high-surface area MgO. Details of this procedure have been given previously [12].

A set of alkali-promoted A/MgO samples (A = Li, Na, K, or Cs) was prepared by incipient wetness impregnation. The alkali metal A was added to the high-surface area MgO using a hydroxide aqueous solution containing the required A concentration to obtain an A/Mg = 0.008 (molar ratio). In addition, magnesia was promoted with different Li^+ loadings to obtain catalysts with 0.13, 0.3, 0.5, 1.2, and 2.6 wt% of lithium. After incorporation of the promoter A, all samples were dried at 353 K and finally decomposed and stabilized at 773 K for 18 h in flowing N_2. The Li-doped MgO samples were denoted as Li/MgO-x.

2.2. Characterization

The chemical content of Li in Li/MgO-x samples was analyzed by atomic absorption spectrometry (AAS). BET surface areas (Sg) were determined by N_2 adsorption at 77 K in a Nova-1000 Quantachrom sorptometer. The structural properties of solid samples were determined by X-ray diffraction (XRD) using a Shimadzu XD-D1 instrument. The morphology of the samples was determined by scanning electron microscopy (SEM) using a JEOL JSM-35C microscope. Because the samples were insulators, they were treated with a gold coating before analysis.

Catalyst base site densities (n_b) were measured by temperature-programmed desorption (TPD) of CO_2 preadsorbed at room temperature. Samples were pretreated in situ in a N_2 flow at 773 K, cooled to room temperature, and then exposed to a flowing mixture of 3% of CO_2 in N_2 until surface saturation was achieved (5 min). Weakly adsorbed CO_2 was removed by flushing in N_2. Finally, the temperature was increased to 773 K at a ramp rate of 10 K/min. Desorbed CO_2 was converted in CH_4 on a methanation catalyst (Ni/Kieselghur), then analyzed using a flame ionization detector (FID).

The chemical nature of adsorbed surface CO_2 species was determined by infrared (IR) spectroscopy after CO_2 adsorption at room temperature and sequential evacuation at increasing temperatures. Experiments were carried out using an inverted T-shaped cell containing the sample pellet and fitted with CaF_2 windows. Data were collected in a Shimadzu 8500 Fourier transform infrared (FTIR) spectrometer. The absorbance scales were normalized to 20-mg pellets. The samples were pretreated in vacuum at 773 K and cooled to room temperature, after which the spectrum of the pretreated catalyst was obtained. After admission of 5 kPa of CO_2 to the cell at room temperature, the samples were evacuated consecutively at 298, 373, 473, and 573 K, and the resulting spectrum was recorded at room

temperature. Spectra of the adsorbed species were obtained by subtracting the catalyst spectrum.

2.3. Catalytic testing

The cross-aldol condensation of citral, CIT (Millennium Chemicals, 95% geranial + neral) with acetone, DMK, (Merck, p.a.) was carried out at 353 K under autogenous pressure ($\approx$250 kPa) in a batch PARR reactor, using an acetone/citral = 49 (molar ratio) and a catalyst/(citral + acetone) = 1 wt% ratio. First, the liquid reactants were introduced, and then the reactor was flushed with nitrogen. Catalysts were pretreated ex situ in flowing N_2 at 773 K for 2 h to remove adsorbed water and carbon dioxide, and then quickly transferred to the reactor without exposing them to air. The batch reactor was assumed to be perfectly mixed. Interparticle and intraparticle diffusional limitations were verified as negligible. Reaction products were analyzed by gas chromatography in a Varian Star 3400 CX chromatograph equipped with a FID and a Carbowax Amine 30 M capillary column. Thirteen samples of the reaction mixture were extracted and analyzed during the 6-h reaction. The main reaction product of citral conversion was PS (*cis*- and *trans*-isomers). Trace amounts of unidentified heavy compounds probably coming from self-condensation of citral were also obtained. Diacetone alcohol (DAA) and mesityl oxide (MO) from self-condensation of acetone were also detected in the reaction mixture.

Selectivities of citral-derived products (S_j, mol of product j/mol of citral reacted) were calculated as S_j (%) = $C_j \times 100 / \sum C_j$, where C_j is the concentration of product j. Product yields (η_j, mol of product j/mol of citral fed) were calculated as $\eta_j = S_j X_{Cit}$, where X_{Cit} is the citral conversion. Similar calculations apply for acetone-derived products.

In additional tests, the self-condensation of acetone was carried out at 353 K under autogenous pressure, loading the reactor with pure acetone. The catalyst/acetone ratio was 1.1 wt%. The main reaction products of acetone conversion were DAA and MO.

3. Results and discussion

3.1. Selection of the alkaline metal promoter

We performed preliminary catalytic tests to compare the effect of the nature of promoter IA on MgO activity and selectivity for PS synthesis by cross-aldol condensation of citral with acetone. All the A/MgO samples (A: Li, Na, K, or Cs) were prepared by impregnation of MgO with a similar A/Mg molar ratio (close to 0.008). Catalytic results are given in Table 1. The addition of Li increased the PS yield of parent MgO, whereas the presence of K or Cs was clearly detrimental to PS formation. The PS yield on Na/MgO was similar to that of MgO, but an effect of the slightly higher promoter concentration on this sample cannot be excluded.

The results of Table 1 can be explained by considering that with the exception of Li^+, the alkaline cations have a larger

Table 1
Composition, surface area and catalytic results of A/MgO and MgO catalysts[a]

Cata- lyst	A^+ loading[b]		$-q_O$ in A_2O	Surface area, Sg (m^2/g)	Citral con- version, X_{Cit}[c] (%)	PS yield, η_{PS}[c] (%)
	(wt%)	A/Mg (molar ratio)				
MgO	0.00	–	–	149	86	82
Li/MgO	0.13	0.008	0.80	138	89	85
Na/MgO	0.59	0.010	0.81	94	87	82
K/MgO	0.81	0.008	0.89	83	66	64
Cs/MgO	2.70	0.008	0.94	70	53	40

[a] $T = 353$ K, $n^0_{DMK} = 0.8$ mol, $n^0_{Cit} = 0.016$ mol, $W_{Cat} = 0.5$ g.
[b] By AAS.
[c] At 6 h.

Table 2
Chemical, textural and structural characterization of Li/MgO-*x* and MgO catalysts

Catalyst	Li^+ loading[a]		Surface area, Sg (m^2/g)	Pore volume (mL/g)	XRD analysis	
	(wt%)	Li/Mg (molar ratio)			Lattice parameter, a (Å)	Crystal- lite size (Å)
MgO	0.00	–	149	0.27	4.199	83
Li/MgO-1	0.13	0.008	138	–	4.201	107
Li/MgO-2	0.30	0.017	100	0.23	4.213	109
Li/MgO-3	0.50	0.029	87	0.25	4.208	114
Li/MgO-4	1.20	0.070	66	0.18	4.216	125
Li/MgO-5	2.60	0.151	56	0.13	4.213	139

[a] By AAS.

ionic radius than Mg^{2+}, and the resulting A_2O oxides are increasingly bulkier as the atomic weight of A increases. The oxygen negative partial charge ($-q_O$) in the A_2O oxides, calculated from the electronegativity equalization principle [13], increases when going from Li_2O to Cs_2O, and the basicity of the oxide promoter increases in the same direction. Even though the basicity increases from Li_2O to Cs_2O, the presence of bulky A_2O species, such as K_2O or Cs_2O, on the MgO surface is detrimental to PS synthesis because they block the catalyst pores, thereby decreasing both the solid surface area and the citral conversion.

The superior catalytic performance observed here for Li/MgO is consistent with our previous finding that Li/MgO is more efficient in promoting gas-phase base-catalyzed reactions compared with the other alkali-modified MgO catalysts [12,14]. Therefore, we selected Li to promote MgO and prepared and characterized several Li/MgO samples with different Li loadings, to investigate the effect of Li concentration on catalyst activity and selectivity for the liquid-phase cross-aldol condensation of citral with acetone.

3.2. Chemical, textural, and structural characterization of Li-promoted MgO catalysts

The chemical composition, BET surface area, pore volume, and XRD analysis results of MgO and Li-promoted MgO samples are given in Table 2. Elemental analysis of the oxides revealed Li loadings ranging between 0.13 and 2.6 wt%. After hydration of commercial MgO and subsequent decomposition
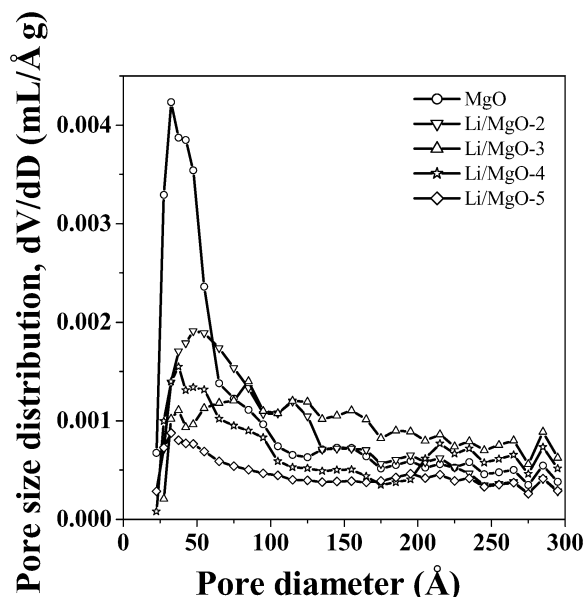
Fig. 1. Pore size distribution profiles of MgO and Li/MgO-*x* catalysts.
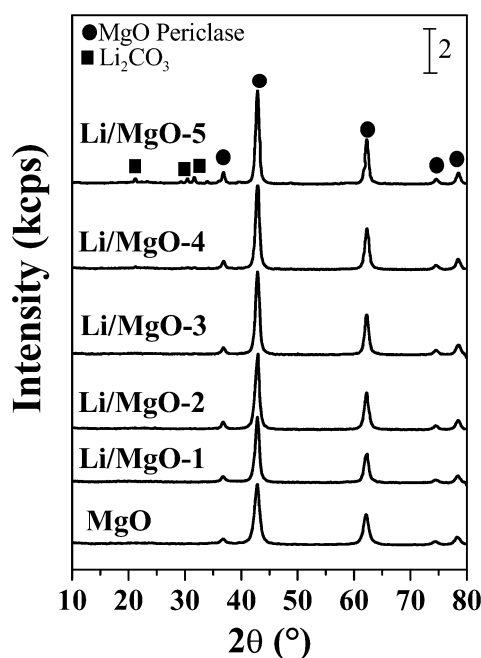

Fig. 2. X-Ray diffraction patterns of MgO and Li/MgO-*x* catalysts.

at 773 K, the BET surface increased from 27 to 149 m^2/g, but promotion of MgO with Li decreased the catalyst surface area (Table 2). Qualitatively, a similar decrease in MgO surface area during promotion with IA metals was reported previously [12, 14]. Pore volume and pore size distribution were also affected by Li doping (Fig. 1). MgO had a pore volume of 0.27 mL/g and a mean pore diameter of about 35 Å, but in the Li/MgO-*x* samples, pore volume decreased with Li content (Table 2).

XRD analysis of Li/MgO-*x* catalysts revealed that a single phase of MgO periclase (ASTM 4-0829) was present at low Li loadings (Fig. 2). No crystalline Li-containing phase was detected by XRD in these samples; however, an incipient Li$_2$CO$_3$ phase was observed in the Li/MgO-5 sample, which contained

2.6 wt% Li (Fig. 2). The unit cell parameter *a* for the MgO structure with face-centered cubic symmetry was calculated from the diffractograms in Fig. 2 for the Li/MgO-*x* catalysts; the *a* values thus obtained are given in Table 2. The ionic radius of Li$^+$ in Li$_2$O ($r_{Li^+} = 0.73$ Å) is slightly smaller than that of Mg^{2+} in MgO ($r_{Mg^{2+}} = 0.86$ Å); therefore, substitution of Li$^+$ for Mg^{2+} in the periclase structure may occur, causing contraction of the MgO lattice and formation of strongly basic anionic vacancies. However, the *a* values of Table 2 are almost constant, indicating no detectable structural modification of the MgO lattice by Li doping. These results suggest that the Li promoter is located on the surface of Li/MgO-*x* samples rather than in the MgO matrix, probably forming small domains of amorphous Li$_2$O or crystalline Li$_2$CO$_3$.

The crystallite sizes of the MgO phase in the MgO and Li/MgO-*x* catalysts were determined from XRD patterns of Fig. 2 using the Scherrer equation for the reflection at $2\theta = 42.7°$ and are given in Table 2. MgO crystallite size increased with increasing Li loading, in line with the concomitant drop in the sample surface area observed in Table 2 and also with results obtained from SEM characterization. In fact, the SEM micrographs in Fig. 3 show that MgO synthesized from Mg(OH)$_2$ (Fig. 3A) has a flake morphology, whereas the Li/MgO-*x* samples have particles with a flat, smoother appearance. These characteristics become more evident as the Li loading increases from 0.5 wt% in Li/MgO-3 (Fig. 3B) to 2.6 wt% in Li/MgO-5 (Fig. 3C).

The crystal size increase, the drop of surface area and pore volume, as well as the morphological changes toward a smoother appearance as the Li content increases are probably a result of particle agglomeration in the presence of the Li salt during MgO aqueous impregnation and further thermal decomposition of the resulting Li(OH)/Mg(OH)$_2$ solid, which involves Li(OH) melting [15].

3.3. Surface acid–base properties of Li/MgO catalysts

The surface base properties of the Li/MgO-*x* samples were investigated by combining TPD and IR measurements of CO$_2$ preadsorbed at room temperature. We measured the CO$_2$ adsorption site densities and binding energies by TPD of CO$_2$; Fig. 4 shows the CO$_2$ desorption rate as a function of desorption temperature for MgO and the Li/MgO-*x* catalysts. The total amount of desorbed CO$_2$ (n_b) was measured by integration of TPD curves; the resulting values are reported in Table 3. Here n_b has a maximum value of 11.3 μmol/m^2 at a Li loading of 0.5 wt% and clearly decreases at higher Li loadings. The base site density increase up to a Li content of 0.5 wt% may be explained by taking into account that the basicity of an oxide surface is related to the electro-donating properties of the combined oxygen anions, so that the higher the partial negative charge on the combined oxygen anions, the more basic the oxide. Thus, the oxygen partial negative charge ($-q_O$) would reflect the electron donor properties of the oxygen in single-component oxides. The $-q_O$ value of Li$_2$O, is 0.8, whereas that of MgO is 0.5; therefore, surface promotion with more
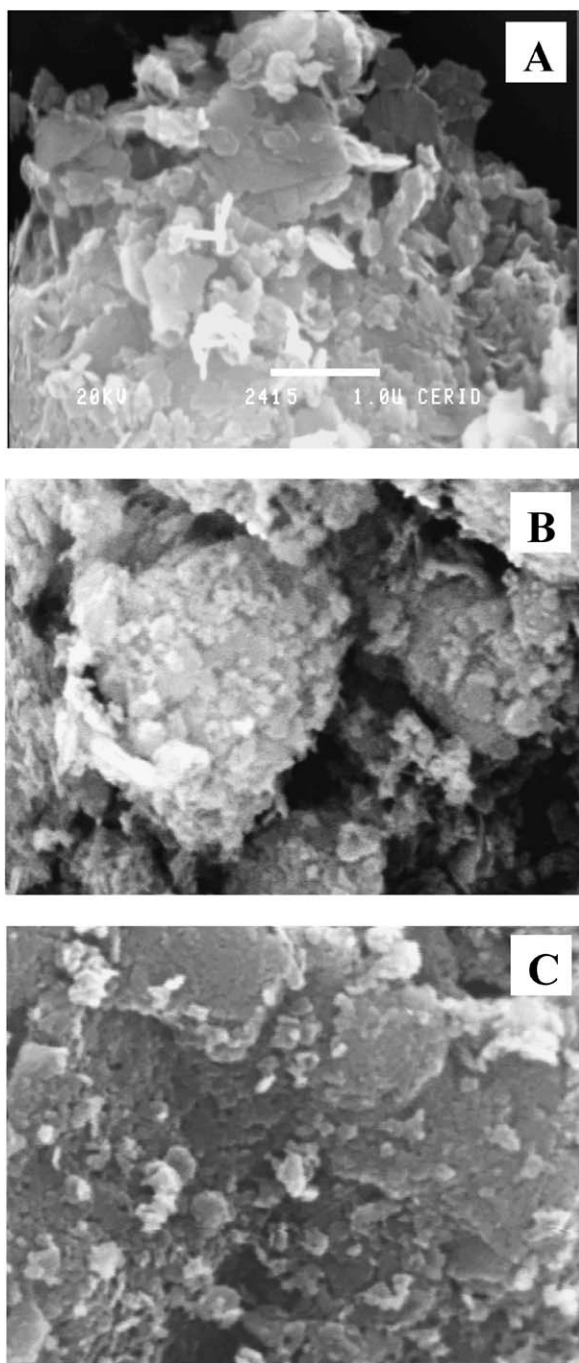
Fig. 3. SEM micrographs of MgO (A); 0.5 wt% Li/MgO (B); 2.6 wt% Li/MgO (C).

Fig. 4. TPD of CO_2 on MgO and Li/MgO-x catalysts.

Table 3
Surface base site properties of MgO and Li/MgO-x samples

Catalyst	Base site density[a] (μmol/m^2)			
	Total n_b	Weak n_{OH}	Medium n_{MO}	Strong n_O
MgO	3.8	0.5	1.8	1.5
Li/MgO-1	5.6	0.8	2.4	2.3
Li/MgO-2	8.5	1.1	2.8	4.6
Li/MgO-3	11.3	1.8	3.0	6.4
Li/MgO-4	8.3	0.5	2.1	5.7
Li/MgO-5	7.1	0.7	0.9	5.5

[a] By TPD of CO_2.

basic Li_2O oxide would be expected to increase the basicity of MgO.

The complex TPD profiles in Fig. 4 suggest that the surfaces of the Li/MgO-x oxides are nonuniform and contain several species formed by CO_2 adsorption; in other words, the sample surfaces contain oxygen atoms of different chemical nature that bind CO_2 with different coordination and binding energy. In previous work [14], we investigated the chemical nature of the adsorbed species on similar alkaline-promoted MgO catalysts using FTIR and identified at least three different CO_2 adsorption species: unidentate carbonate, bidentate carbonate,
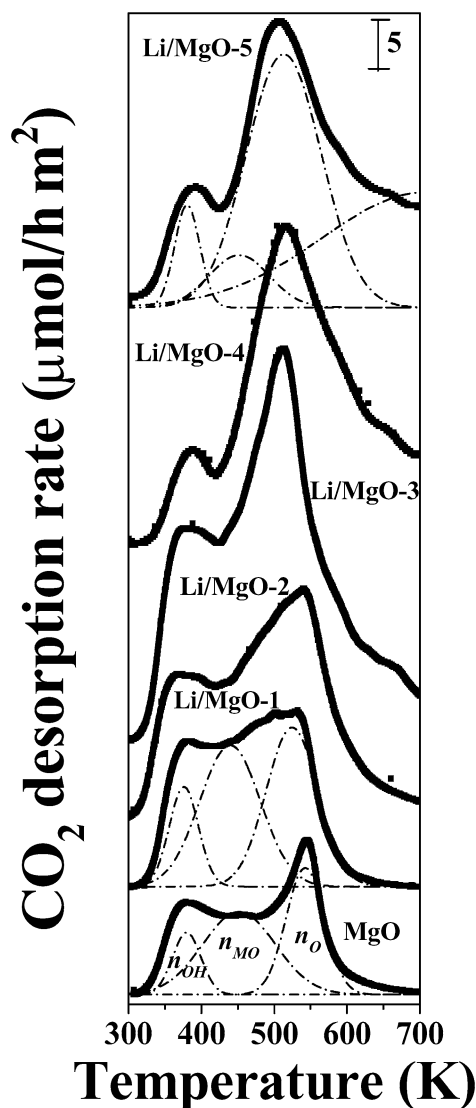
and bicarbonate. These three adsorption species on MgO are depicted in Scheme 2A. Unidentate carbonate formation requires isolated surface O^{2-} ions (i.e., low-coordination anions, such as those present in corners or edges) and exhibits a symmetric O–C–O stretching at 1360–1400 cm^{-1} and an asymmetric O–C–O stretching at 1510–1560 cm^{-1}. Bidentate carbonate forms on Lewis acid–Brönsted base pairs (M^{n+}–O^{2-} pair site, where M^{n+} is the metal cation Mg^{2+} or Li^+), and
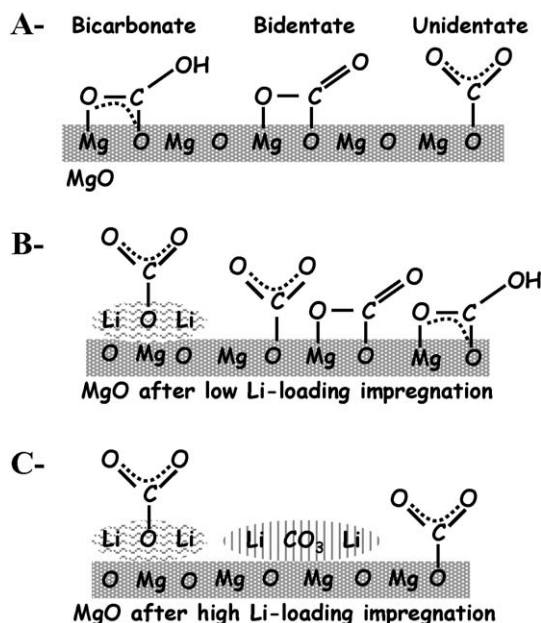
Scheme 2. CO_2 surface species on MgO and on MgO modified by low and high Li loading impregnation.

shows a symmetric O–C–O stretching at 1320–1340 cm^{-1} and an asymmetric O–C–O stretching at 1610–1630 cm^{-1}. Bicarbonate species formation involves surface hydroxyl groups and shows a C–OH bending mode at 1220 cm^{-1}, as well as symmetric and asymmetric O–C–O stretching bands at 1480 and 1650 cm^{-1}, respectively [16–18]. We also determined the following base strength order for these surface oxygen species: low-coordination O^{2-} anions > oxygen in M^{n+}–O^{2-} pairs > OH groups [14].

Similarly, the structure of the chemisorbed CO_2 species on MgO and Li/MgO-x catalysts was determined by FTIR after CO_2 adsorption at room temperature and sequential evacuation at 298, 373, 473, and 573 K (Fig. 5). In agreement with previous work [14], spectra of Fig. 5 show that OH groups are weak base sites, because bicarbonate bands disappeared after evacuation at 373 K, whereas unidentate and bidentate carbonates remained on the surface at higher temperatures, thereby indicating that low-coordination O^{2-} and oxygen in M^{n+}–O^{2-} pairs, respectively, are stronger base sites. Fig. 5 also shows that not only the base site density, but also the CO_2 binding energy, varies with Li content. In fact, whereas bidentate species prevail on the MgO surface after desorption at 573 K (MgO, spectrum d), with increasing Li content, the CO_2 bands shift to the unidentate carbonate position (Li/MgO-x, spectra d), suggesting the presence of more basic oxygen ions on the surface of the Li/MgO-x samples.

Based on the FTIR results, the TPD profiles of Fig. 4 were deconvoluted in three desorption bands to quantify the density of weak, medium, and strong base sites. The results are presented in Table 3. Although CO_2 desorption follows first-order kinetics, for simplicity we have used Gaussian functions for the deconvolution of the TPD traces. The low-temperature peak at 360–380 K was assigned to bicarbonates formed on weak base OH groups (n_{OH}); the middle-temperature peak at 450 K
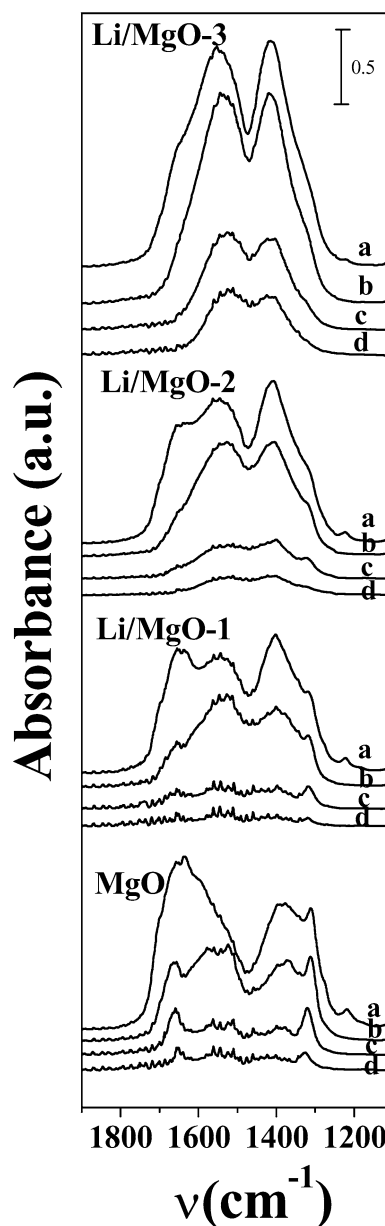

Fig. 5. IR spectra of CO_2 adsorbed at room temperature on MgO and Li/MgO-x catalysts and desorbed at increasing evacuation temperatures: 298 (a), 373 (b), 473 (c), and 573 K (d).

was attributed to bidentate carbonates desorbed from medium-strength metal–oxygen pairs (n_{MO}), and the high-temperature peak at 510–550 K was caused by the release of unidentate carbonates from low-coordination oxygen anions (n_O). A fourth CO_2 desorption peak was observed above 650 K in samples with Li loadings >0.5 wt% (Fig. 4), which can be assigned to incipient decomposition of a reconstructed three-dimensional carbonate. In fact, samples with Li loadings >0.5 wt% form bulk carbonates when exposed to even ambient CO_2, as determined by XRD (Fig. 2). Thus, the area under the peak above 650 K has not been taken into account for quantifying base site density.

Formation of strong base sites was particularly promoted by the addition of Li, so that the relative contribution of strong

base sites (n_O) to the total base site density increased with increasing Li content up to 0.5 wt% Li, essentially at the expense of medium-strength base sites (n_{MO}). For example, strong base sites represent 42% of the total base site density in Li/MgO-1 and 57% in Li/MgO-3.

These CO$_2$ TPD results showing the increase of strong base site density of parent MgO by adding Li up to about 0.5% are in agreement with the IR spectra shown in Fig. 5 that reveal an increasing intensity of the unidentate carbonate bands with increasing Li loading. As shown in Scheme 2B, the surface metal cation M^{n+} participates in the bidentate carbonate adsorption mode, but as the MgO surface is covered by Li$_2$O, the higher $-q_O$ in Li$_2$O compared with that in MgO probably strengthens the C_{CO_2}–$O_{Li/MgO}$ bond and weakens the O_{CO_2}–$M_{Li/MgO}$ bond of the bidentate species, thereby favoring the unidentate adsorption mode without participation of the metal cations [18].

Table 3 also shows that for Li concentrations >0.5 wt%, the base site density diminishes (samples Li/MgO-4 and Li/MgO-5), probably because of the formation of stable lithium carbonates of bulky planar structure [19] that would block the surface Mg^{2+}–O^{2-} pairs that are predominant on unpromoted MgO. This surface transformation with the presence of Li$_2$CO$_3$ is depicted in Scheme 2C.

3.4. Citral/acetone aldol condensation on Li-promoted MgO

The Li/MgO-x samples of Table 3 were tested for the citral/acetone reaction. The reaction formed essentially PSs, and the selectivity to PS was >96% over all of the catalysts after the 6-h catalytic tests. The effect of varying the Li doping on the catalytic performance of the Li/MgO-x catalysts at 353 K is shown in Fig. 6, in which citral conversions (X_{Cit}) are represented as a function of tW/n^0_{Cit}, where t is the reaction time, W is the catalyst weight, and n^0_{Cit} is the initial mol of citral. The local slope of each curve in Fig. 6 gives the citral conversion rate at a specific value of citral conversion and reaction time. Thus, we determined the initial citral conversion rate on an areal basis (r^0_{Cit}, µmol/min m^2) by calculating the initial slopes in Fig. 6 according to

$$r^0_{Cit} = \frac{1}{Sg} \left[\frac{dX_{Cit}}{d(tW/n^0_{Cit})} \right]_{tW/n^0_{Cit}=0} \tag{1}$$

Using a similar procedure, we determined the initial PS formation rate (r^0_{PS}, µmol/min m^2) from the PS yield (η_{PS}) versus tW/n^0_{Cit} curves (not shown here). The r^0_{Cit} and r^0_{PS} values thus obtained for all of the catalysts are given in Table 4. It is observed that r^0_{Cit} and r^0_{PS} increased when small amounts of Li are added, reaching a maximum at ca. 0.5 wt% Li (sample Li/MgO-3). For example, r^0_{PS} increased by a factor of three, from 6.2 µmol/min m^2 on MgO to 20.5 µmol/min m^2 on Li/MgO-3. For Li concentrations > ~0.5 wt%, both r^0_{Cit} and r^0_{PS} decreased. A similar trend with the amount of Li on the catalyst was verified for the PS yield. In fact, Fig. 7 represents the evolution of η_{PS} values obtained at the end of the catalytic runs as a function of the Li loading, and it can be clearly seen that η_{PS} depends on the Li content, reaching a maximum of 93% for about 0.5 wt% Li.

The catalytic results of Table 4 and Figs. 6 and 7 suggest that there is an optimum Li loading, and thus the addition of small amounts of Li improves the MgO activity for PS formation, but Li concentrations > ~0.5 wt% cause the η_{PS} to decrease. The MgO activity increase due to the addition of small amounts of
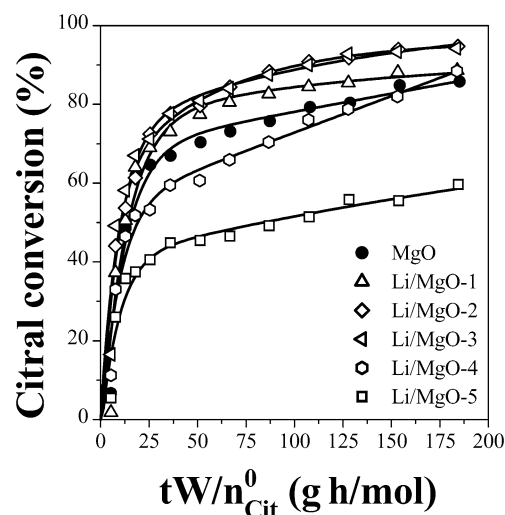

Fig. 6. Citral conversions as a function of parameter tW/n^0_{Cit} for MgO and Li/MgO-x catalysts ($T = 353$ K, $n^0_{DMK} = 0.8$ mol, $n^0_{Cit} = 0.016$ mol, $W_{Cat} = 0.5$ g).
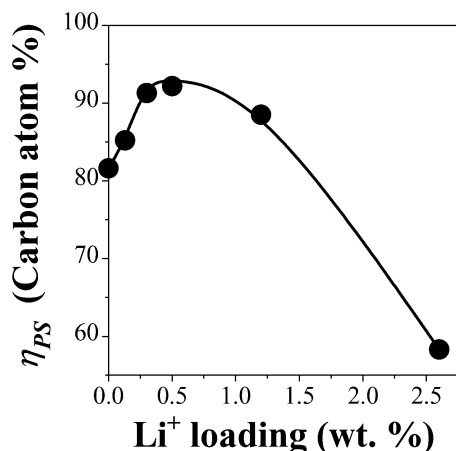
Table 4
Catalytic activity data obtained on Li-promoted MgO samples

Entry	Catalyst	Reaction[a]	Initial citral conversion rate, r^0_{Cit} (µmol/min m^2)	Initial PS formation rate, r^0_{PS} (µmol/min m^2)	Initial DAA formation rate, r^0_{DAA} (µmol/min m^2)	Initial MO formation rate, r^0_{MO} (µmol/min m^2)
1	MgO	Citral/acetone	6.3	6.2	21.1	0.7
2	Li/MgO-1	Citral/acetone	7.8	7.6	26.5	1.4
3	Li/MgO-2	Citral/acetone	15.4	14.9	53.0	1.7
4	Li/MgO-3	Citral/acetone	21.2	20.5	74.7	3.0
5	Li/MgO-4	Citral/acetone	15.7	15.7	50.1	0.5
6	Li/MgO-5	Citral/acetone	15.2	15.2	49.0	<0.1
7	MgO	Acetone/acetone[b]	–	–	18.0	3.8
8	Li/MgO-3	Acetone/acetone[b]	–	–	64.9	32.1

[a] Citral/acetone reaction: $T = 353$ K, $n^0_{DMK} = 0.8$ mol, $n^0_{Cit} = 0.016$ mol, $W_{Cat} = 0.5$ g.

[b] Acetone/Acetone reaction: $T = 353$ K, $n^0_{DMK} = 0.8$ mol, $W_{Cat} = 0.5$ g.

Fig. 7. Pseudoionone yield as a function of Li content ($T = 353$ K, $n_{DMK}^0 = 0.8$ mol, $n_{Cit}^0 = 0.016$ mol, $W_{Cat} = 0.5$ g, $t = 6$ h).
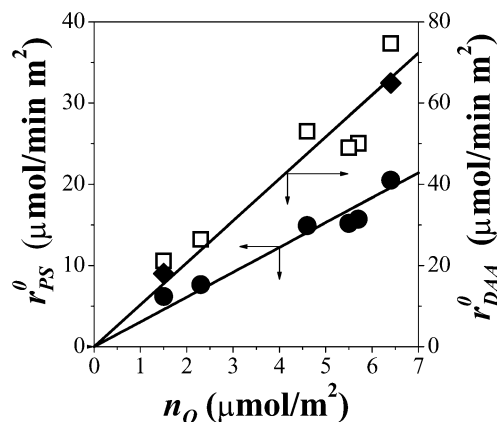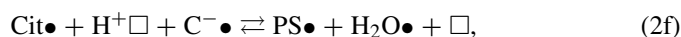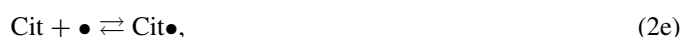

Fig. 8. Initial PS and DAA formation rates on MgO and Li/MgO-x catalysts as a function of strong base site density. PS in citral/acetone reaction (●); DAA in citral/acetone reaction (□); DAA in acetone/acetone reaction (◆). Reaction conditions as in Table 4.
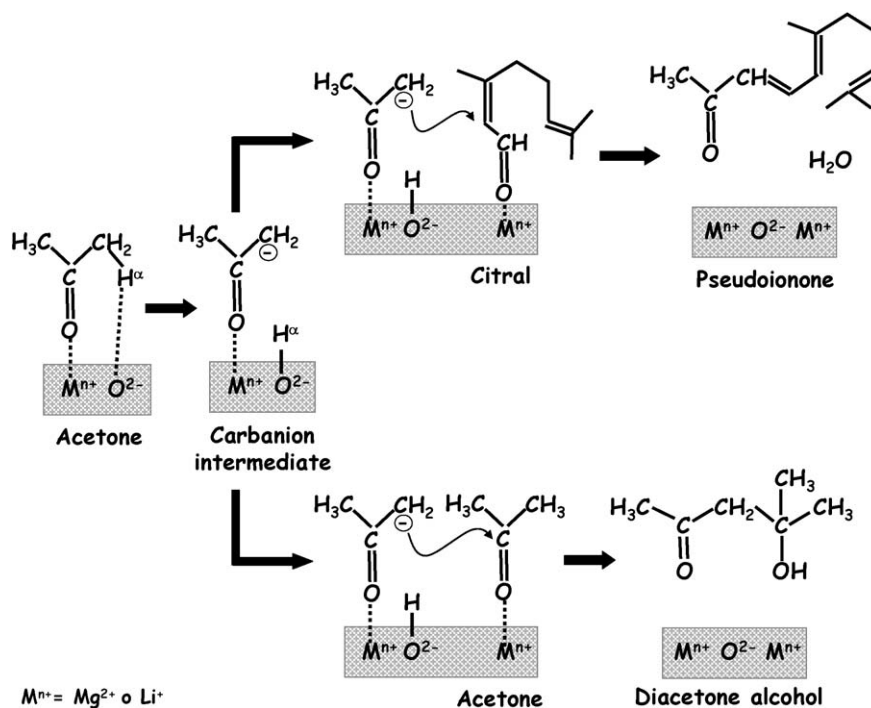
Li is attributed to the spreading of the more basic Li_2O on the MgO surface, which enhances the strong base site density and favors PS formation. In contrast, the presence of stable surface carbonates on MgO doped with high Li concentrations is detrimental to PS synthesis because they block the base sites, as depicted in Scheme 2C.

It is worth noting here that because water is formed during the aldol condensation reactions, we analyzed in several experiments the liquid reaction mixture after the catalytic runs to verify that Li leaching did not take place. Lithium was never detected in the liquid phase, and thus we can rule out any contribution of the homogeneously catalyzed reaction to the catalytic performance of Li/MgO catalysts.

3.5. Surface base properties and mechanism of citral/acetone aldol condensation on MgO and Li/MgO catalysts

To gain insight into the reaction mechanism, and also in an attempt to relate the catalytic behavior of the samples to their surface base properties, we compared the catalyst activity data of Table 4 with the base site densities given in Table 3. We obtained a good correlation between the initial PS formation rate and the density of strong base sites (n_O) as shown in Fig. 8 (closed circles). In contrast, a poor correlation was found when r_{PS}^0 was plotted against the density of weak (n_{OH}) or medium-strength (n_{MO}) basic sites. The observed proportionality between r_{PS}^0 and n_O in Fig. 8 indicates that under initial conditions, the rate-determining step for the PS formation is promoted by strong base sites.

On the other hand, it must be noted that acetone self-condensation is an unavoidable side reaction leading primarily to DAA, which consecutively may dehydrate to MO. Thus, we also determined the initial formation rates of DAA (r_{DAA}^0) and MO (r_{MO}^0); results are given in Table 4. A close inspection of the results of Table 4 shows that r_{DAA}^0 changes with Li content following a similar trend than that observed for r_{PS}^0. In fact, Fig. 8 includes a representation of r_{DAA}^0 as a function of n_O (open squares), and it can be seen that, as in the case of r_{PS}^0, r_{DAA}^0 varies linearly with n_O. The results in Fig. 8 demon-

strate that the strong base sites of the Li/MgO-x catalysts promote the formation of PS and DAA in a similar fashion, thereby suggesting that both products are formed via a common intermediate compound involved in the rate-limiting step of the respective reaction mechanisms.

In general, the basis of any base-catalyzed aldol condensation is the catalyst's ability to abstract the α-proton of one of the reactants. This depends on two factors: the basicity of the active site and the acidity of that proton. The reaction pathway for producing PS from the aldol condensation of citral with acetone, as depicted in Scheme 3, involves the initial abstraction of the α-proton from acetone, forming a carbanion that consecutively attacks the carbonyl group of the contiguously adsorbed citral molecule. The α-proton is the most acidic site of the acetone molecule, with a pK_a of 20 [20]. Then a β-hydroxyl ketone intermediate is expected to form; however, this was never observed among the reaction products under the reaction conditions of this work. Therefore, this unstable intermediate is assumed to rapidly dehydrate [6], forming PS and water and regenerating the active sites on the catalyst surface. In a parallel pathway, the carbanion intermediate formed from acetone might attack a second acetone molecule leading to DAA (Scheme 3).

Based on the foregoing experimental observations, the simultaneous synthesis of PS and DAA on our Li/MgO-x samples can be represented by the following sequence of elementary steps:

$$DMK + \bullet \rightleftarrows DMK\bullet, \tag{2a}$$

$$DMK\bullet + \square \rightleftarrows C^- \bullet + H^+\square, \tag{2b}$$

$$DMK\bullet + H^+\square + C^-\bullet \rightleftarrows DAA\bullet + \bullet + \square, \tag{2c}$$

$$DAA\bullet \rightleftarrows DAA + \bullet, \tag{2d}$$

$$Cit + \bullet \rightleftarrows Cit\bullet, \tag{2e}$$

$$Cit\bullet + H^+\square + C^-\bullet \rightleftarrows PS\bullet + H_2O\bullet + \square, \tag{2f}$$

$$PS\bullet \rightleftarrows PS + \bullet, \tag{2g}$$

$$H_2O\bullet \rightleftarrows H_2O + \bullet, \tag{2h}$$

Scheme 3. Surface process for the citral/acetone aldol condensation.

where ● represents a metal cation, Mg^{2+} or Li^+, □ represents an oxygen anion, and C^- is the carbanion formed from acetone. The functions of weak Lewis acid sites (Mg^{2+} and Li^+ cations) are to provide an adsorption site for both reactants through their carbonyl groups and to stabilize reaction intermediates.

The formation of DAA and PS in the mechanism represented by steps (2a)–(2h) proceeds via parallel reaction pathways that share the common carbanion intermediate, as indicated in steps (2c) and (2f). Based on the proportionality between r_{PS}^0 and r_{DAA}^0 with n_O observed in Fig. 8, the rate-determining step should be shared by both DAA and PS formation pathways and should involve base sites of a strongly basic nature; in the reaction mechanism that corresponds to step (2b). Additional support for the assumption that carbanion formation of step (2b) is the rate-limiting step in the formation mechanism of both PS and DAA was obtained by testing MgO and Li/MgO-3 for the liquid-phase self-condensation of acetone in the absence of citral, for which only elementary steps (2a)–(2d) apply. The results, presented in entries 7 and 8 of Table 4, show that r_{DAA}^0 was about 3.6 times higher on Li/MgO-3 than on MgO, similar to the r_{DAA}^0 increase obtained on the same samples for the citral/acetone reaction (Table 4, entries 4 and 1). Furthermore, when the r_{DAA}^0 values of entries 7 and 8 of Table 4 were plotted in Fig. 8, the experimental data points (closed diamonds in Fig. 8) fit the correlation previously found for the citral/acetone reaction, thereby confirming the participation of strong base sites in the rate-determining step of the acetone/acetone reaction.

Table 4 also shows that the MO formation rate is clearly lower in the citral/acetone reaction (entries 1 to 6) than in acetone/acetone condensation (entries 7 and 8). This result provides evidence of the competitive adsorption between citral and DAA; when citral is present in the reaction mixture, it competes with DAA for the surface Lewis sites (metal cations), and, consequently, the DAA dehydration leading to MO by readsorption through the OH group is inhibited.

The expression for the initial PS formation rate can be derived from the postulated Langmuir–Hinshelwood–Hougen–Watson mechanism considering the carbanion formation of step (2b) as the rate-determining step, as follows:

$$r_{PS}^0 = \frac{k_2 K_{DMK} n_M n_O y_{DMK}^0}{[1 + K_{Cit} y_{Cit}^0 + K_{DMK} y_{DMK}^0]}, \tag{3}$$

where k_2 is the forward kinetic constant of step (2b); K_{DMK} and K_{Cit} are the equilibrium adsorption constants for DMK and citral, respectively; y_{DMK}^0 and y_{Cit}^0 are the molar fractions of DMK and citral in the reactant mixture, respectively; and n_M and n_O are the total density of metal cations and of strongly basic oxygen anions, respectively. In agreement with the catalytic results shown in Fig. 8, Eq. (3) predicts a linear dependence of r_{PS}^0 with n_O. Equation (3) also predicts a negative order with respect to citral, consistent with previous findings that high concentrations of citral strongly inhibit the citral/acetone reaction [8].

To obtain further support for the validity of Eq. (3) in interpreting the catalytic data, we performed additional catalytic tests of the citral/acetone reaction on MgO by changing y_{DMK}^0 while maintaining both y_{Cit}^0 and the catalyst/citral weight ratio constant. Equation (3) can be rearranged as

$$\frac{y_{DMK}^0}{r_{PS}^0} = \frac{1 + K_{Cit} y_{Cit}^0}{k_2 K_{DMK} n_M n_O} + \frac{1}{k_2 n_M n_O} y_{DMK}^0, \tag{4}$$

which predicts a linear dependence between y_{DMK}^0 / r_{PS}^0 and y_{DMK}^0. Precisely, we see that our catalytic data obtained on
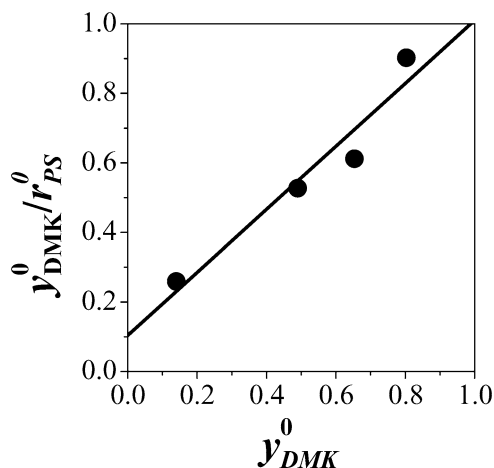
Fig. 9. Kinetics of citral/acetone reaction: Effect of the acetone molar fraction (MgO, $T = 353$ K, $y_{Cit}^0 = 0.02$, $W_{Cat} = 0.356$ g).

MgO show a good linear fit when they are represented in a plot of y_{DMK}^0/r_{PS}^0 versus y_{DMK}^0 (Fig. 9).

In summary, catalytic results for the synthesis of PS via citral/acetone aldol condensation on Li-doped MgO catalysts can be consistently explained by considering that the rate-limiting step of the reaction mechanism is the abstraction of proton H^α from the acetone molecule that would be essentially promoted by the catalyst's strong base sites.

Finally, we remark that precisely because of their strong basicity, low-coordination oxygen anions are very reactive and may reconvert to surface OH^- in the presence of water formed during PS synthesis. Thus, the formation of PS on Li-doped MgO may be accompanied by the gradual modification of the catalyst surface, by reconverting strong O^{2-} basic sites to weak OH^- basic groups. Although it was not the intent of this work to ascertain the changes of the active site nature during reaction, it is noteworthy that eventual changes on the catalyst surface with reaction time would not affect the interpretation of the experimental results given in Table 4 and Fig. 8 obtained at initial reaction conditions.

4. Conclusions

MgO- and Li-doped MgO catalysts efficiently promote the liquid-phase synthesis of PS by aldol condensation of citral and acetone. Li/MgO oxides containing up to about 0.5 wt% Li are better catalysts than MgO, because promotion with Li particularly increases the density of very reactive strong base sites (low-coordination oxygen anions). Higher Li loadings cause particle agglomeration and structural and surface transformations, with formation of unreactive carbonates that block the active sites. Other alkaline metals of larger ionic radius than Li

seem to block the catalyst pores of MgO, with the subsequent decrease of citral conversion and PS yield.

PS synthesis proceeds on MgO and Li/MgO catalysts through a reaction mechanism involving strong base sites that detach the α-proton from the acetone molecule and form a carbanion intermediate in the rate-determining step. The citral/acetone reaction mechanism also involves the participation of weak Lewis acid sites (Mg^{2+} and Li^+), which provide the surface sites needed to adsorb both reactants and to stabilize reaction intermediates. The simultaneous formation of diacetone alcohol from the self-condensation of acetone occurs via parallel reaction pathways that share with the PS formation mechanism both, the carbanion intermediate and the rate-limiting step. Consequently, the diacetone alcohol formation rate is also preferentially promoted on strong base sites.

References

[1] P.Z. Bedoukian, Perfumery and Flavoring Synthetics, Elsevier, New York, 1967, p. 99.
[2] A. Chauvel, B. Delmon, W.F. Holderich, Appl. Catal. A 115 (1994) 173.
[3] Ullman's Encyclopedia of Industrial Chemistry, sixth ed., 2002, electronic release.
[4] P. Gradeff, US Patent 3 840 601 (1974), to Rhodia Inc.
[5] P. Mitchell, US Patent 4 874 900 (1989), to Union Camp Corporation.
[6] M.J. Climent, A. Corma, S. Iborra, A. Velty, Catal. Lett. 79 (2002) 157.
[7] C. Noda Perez, C.A. Henriques, O.A.C. Antunes, J.L.F. Monteiro, J. Mol. Catal. A 233 (2005) 83.
[8] J.C. Roelofs, A.J. van Dillen, K.P. de Jong, Catal. Today 60 (2000) 297.
[9] M.J. Climent, A. Corma, S. Iborra, K. Epping, A. Velty, J. Catal. 225 (2004) 316.
[10] S. Abelló, F. Medina, D. Tichit, J. Pérez-Ramírez, X. Rodríguez, J.E. Sueiras, P. Salagre, Y. Cesteros, Appl. Catal. A 281 (2005) 191.
[11] E.L. Jablonski, I.M.J. Vilella, S.C. Maina, S.R. de Miguel, O.A. Scelza, Catal. Commun. 7 (2005) 18.
[12] J.I. Di Cosimo, V.K. Díez, C.R. Apesteguía, Appl. Catal. A 137 (1996) 149.
[13] R.T. Sanderson, Chemical Bonds and Bond Energy, second ed., Academic Press, New York, 1976, p. 75.
[14] V.K. Díez, C.R. Apesteguía, J.I. Di Cosimo, Catal. Today 63 (2000) 53.
[15] V. Perrichon, M.C. Durupty, Appl. Catal. 42 (1988) 217.
[16] R. Philipp, K. Fujimoto, J. Phys. Chem. 96 (1992) 9035.
[17] C. Morterra, G. Ghiotti, F. Boccuzzi, S. Coluccia, J. Catal. 51 (1978) 299.
[18] T. Kanno, M. Kobayashi, in: M. Misono, Y. Ono (Eds.), Acid–Base Catalysts, vol. II, Kodansha/Elsevier, Tokyo, 1994, p. 207.
[19] A. Grzechnik, P. Bouvier, L. Farina, J. Solid State Chem. 173 (2003) 13.
[20] H.O. House, Modern Synthetic Reactions, second ed., Benjamin-Cummings Pub. Co., Menlo Park, 1972, p. 494.